Reconciling Ground Motions and Stress Drops for Induced Earthquakes in the Western Canada Sedimentary Basin

Joanna M. Holmgren*[1], Gail M. Atkinson[1], and Hadi Ghofrani[1]

ABSTRACT

A regional ground-motion prediction equation (GMPE) is defined for earthquakes in the western Canada sedimentary basin. The stress parameter model that is input to the GMPE, which controls high-frequency amplitudes, is developed based on an empirical Green's function (EGF) study in the same region (Holmgren *et al.*, 2019). The GMPE is developed using the generic GMPE approach of Yenier and Atkinson (2015a,b); regional parameters, including attenuation and site response, are calibrated using a database of response spectra. The ground-motion database comprises 726 records from 92 earthquakes with magnitudes 2.3–4.4, at distances to 200 km; most events are believed to be related to hydraulic fracturing. To investigate discrepancies between the values of GMPE stress parameter and EGF stress drop for individual earthquakes, stress parameters are computed for each event by fitting the GMPE to observed response spectra. There is a large scatter in the EGF versus GMPE stress estimates, even though the GMPE estimates were implicitly calibrated to equal the EGF values on average. The discrepancies can be attributed to two methodological factors. First, the EGF approach removes the site and path terms through spectral division, whereas the GMPE approach relies on an average regional model as determined from regression of the source and path attenuation. The use of an average regional model results in greater uncertainty, in particular, due to directivity effects (which are better accommodated in the EGF approach). Second, the EGF approach is performed in the Fourier domain, whereas the GMPE fitting is done in the response spectral domain. We conclude that EGF stress-drop models provide useful constraints for GMPE development, when used in combination with calibration to a ground-motion database.

KEY POINTS

- We reconcile stress-drop estimates from EGF studies with those inferred from GMPEs.
- GMPEs have limited capability to model source effects such as directivity, relative to the EGF approach.
- The corner frequency from EGF studies can be used to predict high-frequency ground motions, with caveats.

Supplemental Material

INTRODUCTION

The earthquake source parameter widely referenced as the stress drop ($\Delta\sigma$) is plagued by many definitions and many conventions for its determination. Initially, it was intended as a static measure describing the total stress release of an earthquake rupture. Its determination in this context is based on the estimation of the rupture area's slip and dimensions (e.g., Eshelby, 1957). The stress drop became a parameter of interest in the development of ground-motion prediction equations (GMPEs, also called ground-motion models) from the 1980s onward (Hanks, 1979; Hanks and McGuire, 1981; Boore, 1983; Toro and McGuire, 1987; Atkinson and Boore, 1997, 2006; Campbell, 2003). Many approaches to the development of GMPEs, including the stochastic approach (e.g., Boore, 2003) and the hybrid empirical approach (e.g., Campbell, 2003; Pezeshk *et al.*, 2018), tie the amplitude of high-frequency ground motions to the Brune (1970) source model. Under the Brune model, the amplitude of the Fourier acceleration spectrum at low frequencies is controlled by the seismic moment (M_0). The amplitude rises with the square of

1. Department of Earth Sciences, University of Western Ontario, London, Ontario, Canada

*Corresponding author: joannamholmgren@gmail.com

Cite this article as Holmgren, J. M., G. M. Atkinson, and H. Ghofrani (2020). Reconciling Ground Motions and Stress Drops for Induced Earthquakes in the Western Canada Sedimentary Basin, *Bull. Seismol. Soc. Am.* **XX**, 1–13, doi: 10.1785/0120190308

frequency to the corner frequency (f_c), above which the amplitude spectrum is constant. The constant level attained at high frequency is proportional to ($M_0^{1/3} \Delta\sigma^{2/3}$), in which $\Delta\sigma$ can be calculated from f_c (see Brune, 1970; Boore, 2003).

There are several definitions and conventions for determining stress drop. Issues arise when differing definitions are used interchangeably because they are not equivalent (Atkinson and Beresnev, 1997). One common approach relates the far-field value of f_c to the fault dimensions (e.g., Allmann and Shearer, 2009; Huang *et al.*, 2016; Abercrombie *et al.*, 2017; Sumy *et al.*, 2017), where f_c is most often determined from an empirical Green's function (EGF) approach. We denote this definition of the stress drop as $\Delta\sigma_{drop}$. Another well-known definition comes from the engineering seismology perspective (Hanks, 1979; Hanks and McGuire, 1981), wherein stress drop is determined from the high-frequency spectral amplitudes of observed ground motions ($f \gg f_c$). To distinguish it from the definition based on dimensional source attributes inferred from an EGF analysis, the stress defined in this way is often referred to as the stress parameter (e.g., Boore, 2003; Atkinson and Boore, 2006), which we denote $\Delta\sigma_{par}$ herein.

There are a few reasons why $\Delta\sigma_{drop}$ and $\Delta\sigma_{par}$ may differ from each other even if their definitions are entirely consistent. Specifically, $\Delta\sigma_{drop}$ is typically inferred from an EGF analysis conducted in the Fourier domain, whereas $\Delta\sigma_{par}$ describes the ground-motion amplitudes in the response spectral domain. Bora *et al.* (2016) demonstrated that Fourier and response spectra are not linearly related; they scale similarly at low frequencies, but at high frequencies the response spectrum is dependent on both the high- and low-frequency sections of the corresponding Fourier spectrum. Moreover, there are a number of methods and conventions for determining both parameters, which further complicate comparisons.

Holmgren *et al.* (2019) determined corner frequencies and stress drops of 116 earthquakes in the western Canada sedimentary basin (WCSB) using the EGF approach, largely following the methods of Abercrombie *et al.* (2017). The EGF method is seen by many researchers as an advantageous way to retrieve the source spectrum (e.g., Baltay *et al.*, 2010; Onwuemeka *et al.*, 2018; Yoshimitsu *et al.*, 2019). The advantage of the EGF approach is that it avoids the trade-offs involved in simultaneously determining source, path, and site effects using spectral division of the target earthquake by a smaller, collocated earthquake (an EGF earthquake). The spectral division effectively removes the path and site components from the recorded spectrum of the target earthquake, provided that the EGF earthquake shares the same focal mechanism, propagation path, and site effects as the target record. These conditions are commonly satisfied by requiring a high cross-correlation coefficient between the target and EGF earthquakes (e.g., Abercrombie, 2015). Holmgren *et al.* (2019) observed large station-to-station variability in $\Delta\sigma_{drop}$ estimates for many of the study earthquakes in the WCSB, which they attributed to the sparse station coverage coupled with significant rupture directivity effects. Directivity is an important source effect that results in azimuthal variations in recorded ground-motion durations and amplitudes for a single earthquake (Haskell, 1964), and can thus affect $\Delta\sigma_{drop}$ estimates. Directivity results in larger apparent values of f_c and $\Delta\sigma$ in the forward rupture direction and lower values in the backward direction. The directivity effects may average out if the earthquake is recorded over many azimuths, but if the station distribution is sparse, directivity will increase the variability and can lead to bias of $\Delta\sigma_{drop}$.

Hanks (1979) and Hanks and McGuire (1981) advanced a method to determine $\Delta\sigma_{par}$ from ground motions using random vibration theory to relate the root mean square acceleration (a_{rms}) of the acceleration spectrum to peak ground acceleration (PGA). This approach was extended to interpret both peak ground motions and response spectra in the context of the stochastic ground-motion model (Boore, 1983, 2003; Boore *et al.*, 2010) and has been widely applied in the development of stochastic GMPEs (e.g., Toro and McGuire, 1987; Atkinson and Boore, 2006). Boore *et al.* (2010) showed that the value of $\Delta\sigma_{par}$ is very sensitive to the geometric spreading model assumed. Yenier and Atkinson (2015a) attempted to avoid the trade-off between the source and path parameters in their generic GMPE approach using the shape of the observed spectrum to determine $\Delta\sigma_{par}$, instead of its absolute amplitude. Atkinson *et al.* (2015) not only followed a similar approach, but also removed site effects using simultaneous regression to the generic GMPE form.

From a methodological perspective, the EGF approach is the preferred way to obtain information on the source spectrum, because it clearly separates the source effect from those of path and site. However, EGF studies are subject to restrictive data requirements due to their reliance on small collocated earthquakes to use as EGFs. Moreover, if the intended use of the source information is for the prediction of engineering measures of ground motion (i.e., peak amplitudes and response spectra), then it is not clear whether the results of EGF studies are directly applicable. The GMPE approach, by contrast, is versatile and practical, linking its measure of stress directly to ground-motion amplitudes.

In this study, we investigate the use of $\Delta\sigma_{drop}$ as a proxy for $\Delta\sigma_{par}$. The study serves several useful purposes: (1) it defines a region-specific GMPE for the WCSB; (2) it reconciles models of $\Delta\sigma_{drop}$ with observed ground-motion amplitudes at high frequency; (3) it illustrates how published $\Delta\sigma_{drop}$ estimates from the literature can be used to aid in the development of GMPEs; and (4) by comparing the estimates of $\Delta\sigma_{par}$ to the corresponding estimates of $\Delta\sigma_{drop}$ for individual earthquakes, we gain insight into the strengths and weaknesses of these alternative windows into high-frequency ground-motion processes.

DATABASE

The study database is that of Holmgren *et al.* (2019), who used the EGF approach to obtain source parameters for induced

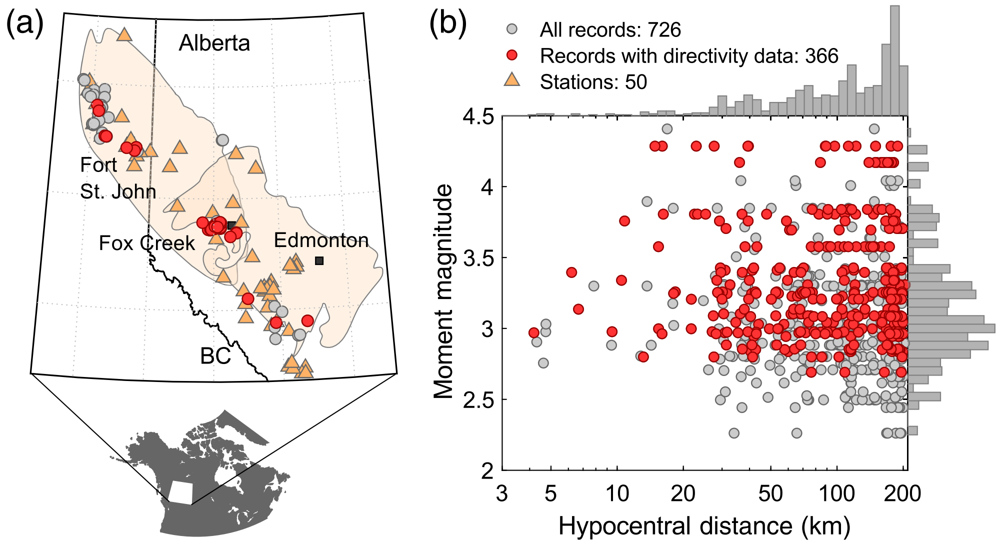

Figure 1. Database of study earthquakes and records. (a) Map of stations (triangles) and study earthquakes (light circles); those with resolvable directivity are shown as dark circles. Shaded region is the western Canada sedimentary basin (WCSB). (b) Record distribution by moment magnitude and distance. The color version of this figure is available only in the electronic edition.

earthquakes in the WCSB; we update it to include two recent events. We use only those earthquakes for which we were able to determine moment magnitude (**M**). The database consists of earthquakes from April 2013 to June 2019, including 92 earthquakes with **M** from 2.3 to 4.4, recorded on stations within 200 km epicentral distance. Most of the events occurred at very shallow depth (<5 km). On the basis of spatiotemporal correlations with proximate oil and gas operations, it is believed that most (~60%) of the events were triggered by hydraulic fracturing (Atkinson *et al.*, 2016). Figure 1 shows an overview map of the region, along with the record distribution in magnitude and distance. The records are three-component broadband seismograms, recording velocity at 100 samples per second. The moment magnitude for each event was determined by fitting the low-frequency level of the displacement spectrum to a Brune (1970) source model, assuming bilinear geometrical spreading with a slope of −1.3 to 50 km and −0.5 thereafter (Yenier and Atkinson, 2015b) and a frequency-independent quality factor $Q = 1000$; we confirmed by analysis of residuals versus distance that this model fits the observed low-frequency attenuation trends.

We band-pass filter all records between 0.1 and 50 Hz using a two-pole, two-pass, Butterworth filter. Next, the signal-to-noise ratio (SNR) is checked by comparing 5 s of *S*-wave recording to pre-*P* noise. Records with SNR ≥ 3 are retained for analysis. Each retained record is corrected to remove instrument response, converted to acceleration, and windowed to start 5 s before the *P*-wave arrival and last for 85 s in total. We compute the 5% damped pseudospectral acceleration (PSA) from the accelerograms using the Nigam and Jennings (1969) algorithm. For records, where both horizontal components passed the SNR check (almost all of the retained records), we compute the horizontal geometric mean response spectrum (geomean PSA). The retained database comprises 726 geomean PSA from 92 earthquakes, recorded on 50 stations. About half of the records come from earthquakes that Holmgren *et al.* (2019) determined to have resolvable directivity effects. Tables S1 and S2 (available in the supplemental material to this article) contain the earthquake parameters and individual PSA records, respectively.

GENERIC GMPE

We use the generic GMPE method (Yenier and Atkinson, 2015a,b) to develop a regionally calibrated stochastic equivalent point-source model for response spectral amplitudes. Our approach follows that of Novakovic *et al.* (2019) in using regression to determine source, path, and site effects within the generic GMPE framework, wherein for each record:

$$\ln Y = F_E + F_Z + F_\gamma + F_S + C, \quad (1)$$

in which Y is the recorded ground motion (in this case, PSA at a specific frequency), F_E is the event term (a frequency-dependent source effect), F_Z is the geometrical spreading term (a frequency-independent path effect), F_γ is the anelastic attenuation (a frequency-dependent path effect), F_S is the site term (frequency-dependent site effect), and C is a frequency-dependent regional calibration factor that encompasses any residual regional effects. F_E consists of two components, which model the source effects of magnitude and stress parameter on ground motions in the response spectral domain:

$$F_E = F_M + F_{\Delta\sigma}, \quad (2)$$

in which F_M describes the magnitude-scaling effect for a Brune (1970) point-source model with constant stress drop of 100 bars, assuming high-frequency attenuation given by kappa (Anderson and Hough, 1984) of $\kappa_0 = 0.025$ s (see Yenier and Atkinson, 2015a,b). $F_{\Delta\sigma}$ describes the stress parameter scaling effect for events with stress values higher or lower than the reference value of 100 bars. The idea behind equation (2) is to separate the effects of magnitude and stress parameter on the scaling of response spectral amplitudes.

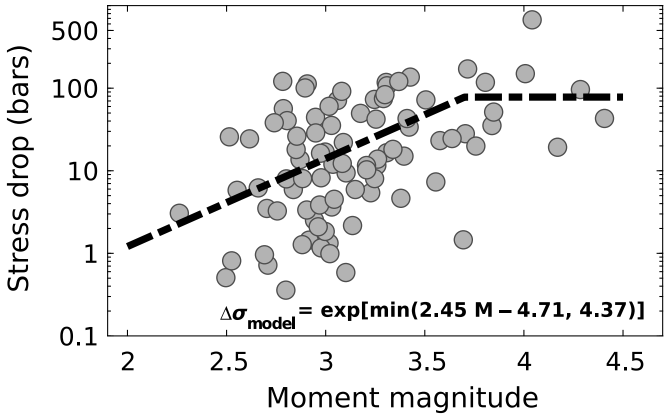

Figure 2. Input stress parameter model $\Delta\sigma_{\text{model}}$ (dashed line) compared to the WCSB stress-drop values from the empirical Green's function (EGF) study of Holmgren *et al.* (2019) (circles).

For simplicity, several of the GMPE components are adopted from previous studies. F_M does not depend on region and is taken directly from Yenier and Atkinson (2015b). We assumed an initial model for $F_{\Delta\sigma}$ that was developed by fitting the Holmgren *et al.* (2019) WCSB EGF stress drops versus magnitude to a simple two-segment line. We scaled the initial best-fit model for the EGF stress drops up slightly (by a factor of 1.3) because we found this was needed to ensure consistency on average between the input stress-drop model and the output stress parameter values; we return to this point later. Figure 2 shows the adopted $F_{\Delta\sigma}$ function. F_Z and F_γ were determined empirically for the WCSB by Novakovic *et al.* (2019). Table 1 contains the functional forms of these components and Table S3 contains the coefficient values. For a detailed description of the methodology and its parameters, see Yenier and Atkinson (2015b) or Novakovic *et al.* (2018).

To fine-tune the generic GMPE to describe our WCSB database, we first convert the Novakovic *et al.* (2019) anelastic attenuation parameter (γ) to the equivalent Q:

$$Q(f) = -\frac{\pi f}{\gamma\beta}, \quad (3)$$

in which f is frequency in hertz and β is the shear-wave velocity in $\mathrm{km \cdot s^{-1}}$. Multiple studies have reported source depths between 3 and 4 km for induced events in the WCSB (e.g., Schultz *et al.*, 2017; Eaton *et al.*, 2018; Wang *et al.*, 2018). Therefore, following Holmgren *et al.* (2019), we assume a constant depth of 4 km and $\beta = 3.2\ \mathrm{km \cdot s^{-1}}$ for all earthquakes (Chen *et al.*, 2015; Wang *et al.*, 2018). The regional seismic Q model can be expressed as

$$Q(f) = \max(120, 271 f^{0.96}), \quad (4)$$

which is then converted back (i.e., through equation 3) to a smoothed function for the γ factor. Figure 3 shows $\gamma(f)$ and $Q(f)$ for the WCSB in comparison to values for three other regions in North America, as determined using the same methodology. Figure 4 displays Q-values reported in other studies in the literature; the methods varied among these studies, but all used similar geometrical spreading functions.

To obtain F_S and C, we compute the residuals of the horizontal geomean PSA (i.e., the difference between the observed

TABLE 1
Generic Ground-Motion Prediction Equation Components

Component	Functional Form	Parameters and References
Magnitude effect, F_M	$F_M = \begin{cases} e_0 + e_1(\mathbf{M} - \mathbf{M}_h) + e_2(\mathbf{M} - \mathbf{M}_h)^2, & \mathbf{M} \le \mathbf{M}_h \\ e_0 + e_3(\mathbf{M} - \mathbf{M}_h), & \mathbf{M} > \mathbf{M}_h \end{cases}$	**M**—moment magnitude; $\mathbf{M}_h$—hinge magnitude (YA15b); e_{0-3}—frequency-dependent coefficients (YA15b)
Stress adjustment, $F_{\Delta\sigma}$	$F_{\Delta\sigma} = e_{\Delta\sigma} \ln(\frac{\Delta\sigma_{\text{model}}}{100})$ $e_{\Delta\sigma} = \begin{cases} s_0 + s_1\mathbf{M} + s_2\mathbf{M}^2 + s_3\mathbf{M}^3 + s_4\mathbf{M}^4, & \Delta\sigma_{\text{par}} \le 100 \text{ bars} \\ s_5 + s_6\mathbf{M} + s_7\mathbf{M}^2 + s_8\mathbf{M}^3 + s_9\mathbf{M}^4, & \Delta\sigma_{\text{par}} > 100 \text{ bars} \end{cases}$ $\Delta\sigma_{\text{model}} = \exp[\min(2.45\ \mathbf{M} - 4.71, 4.37)], 2 \le \mathbf{M} \le 4.5$	$\Delta\sigma_{\text{par}}$—stress parameter (bars); $e_{\Delta\sigma}$—rate of ground-motion scaling (YA15b); s_{0-9}—frequency-dependent coefficients (YA15b); d—depth (km)
Geometrical spreading, F_Z	$F_Z = \ln(Z) + (b_4 + b_5\ \mathbf{M}) \ln(R/R_{\text{ref}})$ $R = \sqrt{D_{\text{rup}}^2 + h^2}$ $R_{\text{ref}} = \sqrt{1 + h^2}$ $h = 10^{-0.405+0.235\ \mathbf{M}}$ $Z = \begin{cases} R^{b_1} & R \le 80 \text{ km} \\ 80^{b_1}(\frac{R}{80})^{b_2} & 80 \text{ km} < R \le 160 \text{ km} \\ 80^{b_1}(\frac{160}{80})^{b_2}(\frac{R}{160})^{b_3} & R > 160 \text{ km} \end{cases}$	Z—geometrical spreading function; b_{1-3}—geometrical spreading rates (NAAG19); b_{4-5}—frequency-dependent coefficients relating Fourier and response domains (YA15b); R—effective distance (km) D_{rup}—closest distance to rupture (km); h—pseudodepth term (km); R_{ref}—reference effective distance (km)
Anelastic attenuation, F_γ	$F_\gamma = \gamma D_{\text{rup}}$	γ—frequency-dependent anelastic attenuation (NAAG19)

NAAG19, Novakovic *et al.* (2019); YA15b, Yenier and Atkinson (2015b).

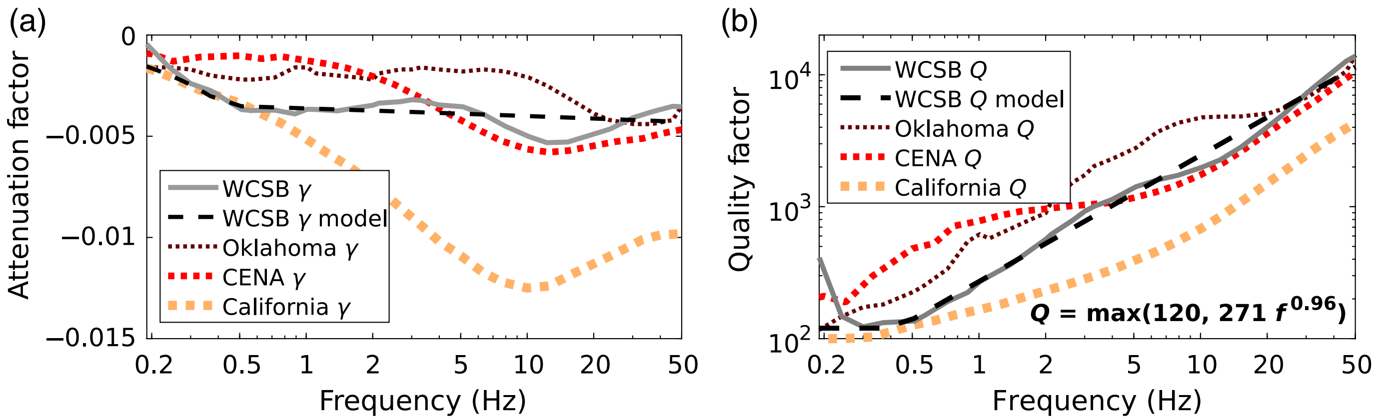

Figure 3. (a) Anelastic attenuation coefficient values γ (solid gray line) and the proposed smoothed model (dashed black line) for the WCSB, in comparison to γ-values from Oklahoma (dark dotted; Novakovic *et al.*, 2018), central and eastern North America (CENA, medium dotted; Yenier and Atkinson, 2015b), and California (light dotted; Yenier and Atkinson, 2015b). (b) Quality factor as determined from γ using equation (3) (same models); equation for the WCSB Q model is given. The color version of this figure is available only in the electronic edition.

and model PSA in natural logarithm units) after removing all other effects. The residual can be expressed as

$$F_s + C = \ln Y - (F_E + F_Z + F_\gamma). \qquad (5)$$

For each station with ≥3 records, the average station residual is computed over all events. C is taken as the mean value of the average station residuals to provide equal weighting to each station. When defined in this way, the factor C can be interpreted as the average regional difference between the site conditions at the stations and those embedded in the generic GMPE of Yenier and Atkinson (2015a,b) and Novakovic *et al.* (2019). These differences are substantial, because most sites in the WCSB are on soil (Farrugia *et al.*, 2017), whereas the reference condition for the generic GMPE is B/C boundary site condition ($V_{S30} = 760$ m/s) with site high-frequency attenuation term kappa $\kappa_0 = 0.025$ s. The station terms F_S provide the difference between the average station residual and C for each station. Figure 5 displays C and F_S for the 50 stations that passed the ≥3 record criterion. Table S4 contains the individual station terms.

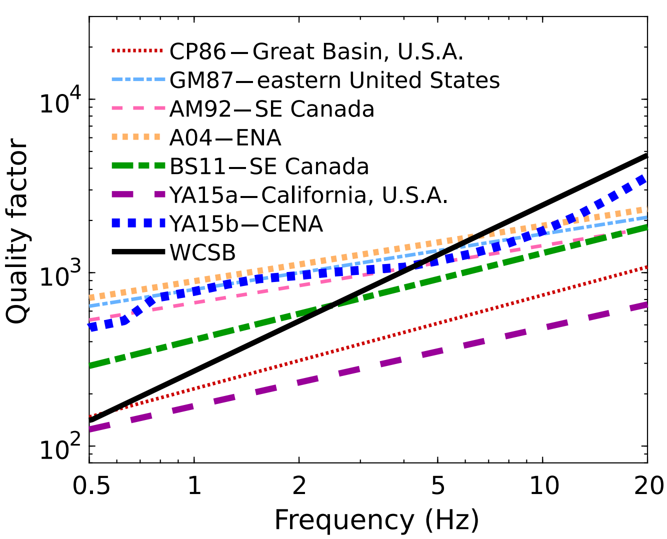

Figure 4. WCSB quality factor (black solid line) compared to Q-values in literature for different regions: CP86, Chávez and Priestley (1986), Great Basin, U.S.A.; GM87, Gupta and McLaughlin (1987), eastern United States; AM92, Atkinson and Mereu (1992), southeastern (SE) Canada; A04, Atkinson (2004), eastern North America (ENA); BS11, Boatwright and Seekins (2011), SE Canada; YA15a, Yenier and Atkinson (2015a), California; YA15b, Yenier and Atkinson (2015b), CENA. The color version of this figure is available only in the electronic edition.

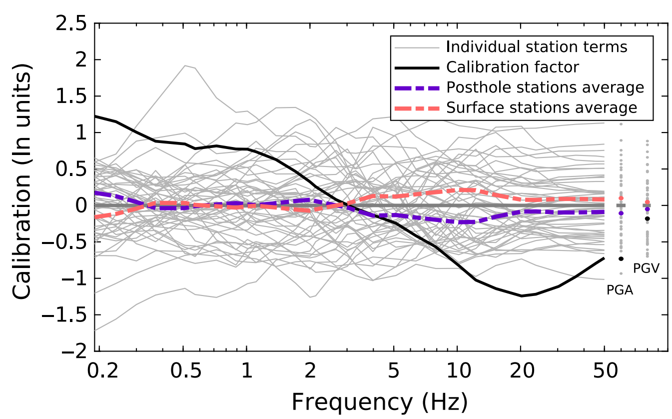

Figure 5. Calibration factor (C, heavy black line) and individual station terms (F_S, light lines) for the 50 stations in this study. The average of all the individual station terms (heavy gray line) is constrained to zero by definition, and thus the calibration factor contains any average regional site response. The average posthole and station terms are shown in dark and light dashed lines, respectively. PGA, peak ground acceleration; PGV, peak ground velocity. The color version of this figure is available only in the electronic edition.

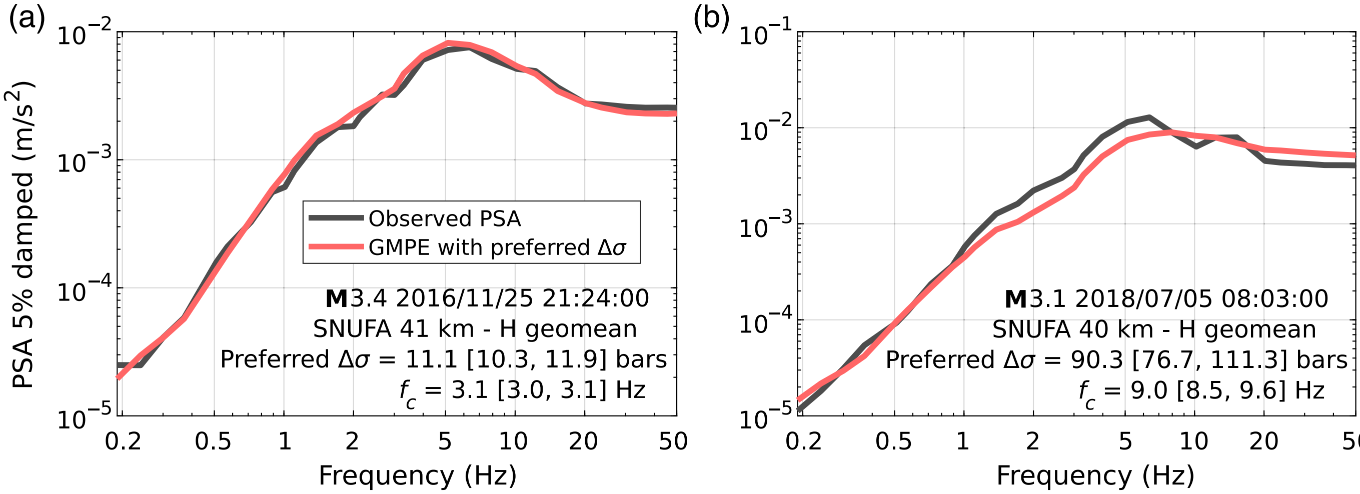

Figure 6. Examples of fitting the ground-motion prediction equation (GMPE, light solid line) to observed data (dark solid line) at station SNUFA for two specific events (a) and (b) (details shown in figure panels). The numbers in brackets show error range on parameters. PSA, pseudospectral acceleration. The color version of this figure is available only in the electronic edition.

STRESS PARAMETER, $\Delta\sigma_{par}$

The stress parameter is contained in F_E, through its $F_{\Delta\sigma}$ component (equation 2 and Table 1). Using the developed regional GMPE, we invert for the best-fitting value of $\Delta\sigma_{par}$ for each record using nonlinear least squares, considering the known values of **M** and distance. We compute the uncertainty in $\Delta\sigma_{par}$ using a grid-search technique to find the perturbation of the best-fit value that results in an increase of variance by 5%.

The stress parameter value can also be expressed in terms of the corresponding corner frequency. The underlying earthquake source model of the generic GMPE assumes a Brune (1970) source model in which $\Delta\sigma_{par}$ is related to the Brune corner frequency f_c through (Eshelby, 1957; Boore, 2003):

$$\Delta\sigma_{par} = \frac{7}{16} M_0 \left(\frac{f_c}{k_{Brune} \times 10^7 \beta} \right)^3 = M_0 \left(\frac{f_c}{4.9 \times 10^6 \beta} \right)^3, \quad (6)$$

in which $\Delta\sigma_{par}$ is in bars, M_0 is the seismic moment in dyn · cm, f_c is in hertz, and k_{Brune} is a constant relating the rupture radius to f_c (in which $k_{Brune} = 0.372$). As for equation (3), we assume a constant focal depth of 4 km and $\beta = 3.2\ \text{km} \cdot \text{s}^{-1}$ for all earthquakes. Equation (6) can be used to convert the $\Delta\sigma_{par}$ values obtained by PSA inversion to f_c values for each record.

Figure 6 shows two examples of the GMPE-fitting process, in which we compare the GMPE for the best-fit stress parameter for a specific record to the observed ground motion. The equivalent corner frequency for the specific record is also indicated. An interesting feature to note in Figure 6 is the relatively low high-frequency spectral amplitudes for typical records in the WCSB. This is reflected in the overall calibration constant C (Fig. 5), which diminishes high-frequency amplitudes relative to those expected for the gradational B/C profile with $\kappa_0 = 0.025$ s that was the basis for the original generic GMPE formulation of Yenier and Atkinson (2015a). We infer a strong influence of high-frequency site attenuation for most sites in the region. Some of this may be due to the relatively soft soils on which many instruments are located. Moreover, many of the WCSB seismometers were installed in postholes at several meters depth, which may significantly dampen high-frequency amplitudes relative to surface installations (Héloïse *et al.*, 2012; Hollender, 2019). This can occur due to destructive interference of the downgoing wave. Hollender (2019) compared the high-frequency amplitudes at a surface station to one buried at 3 m and found a deamplification (factor of 0.7) at 15 Hz. This effect appears in the station terms F_S in Figure 5. When comparing the average F_S of all posthole stations to the average surface station F_S (darker and lighter dashed lines, respectively), it is seen that the postholes tend to have lower values at higher frequencies, indicating less high-frequency content. This will be discussed later.

Finally, we compute the stress parameter for each earthquake. To ensure equivalent comparisons between methods, corner frequency was treated as the basic source parameter. We take the geometric mean of the f_c values at all stations recording an event, then convert it back to $\Delta\sigma_{par}$ through equation (6), to obtain the event-specific values of $\Delta\sigma_{par}$. Using the initial input stress model (solely based on the EGF $\Delta\sigma_{drop}$ values), the individual $\Delta\sigma_{drop}$ and $\Delta\sigma_{par}$ estimates differed on average by a factor of 1.3. Because we wanted a GMPE that produced, on average, $\Delta\sigma_{par}$ similar to $\Delta\sigma_{drop}$ to study their discrepancies, we ensured a 1:1 relationship by adjusting the input model by a factor of 1.3 (Fig. 2). However, both these input stress models resulted in similar residuals. Thus, unless individual $\Delta\sigma_{par}$ estimates are of interest, there is no need to adjust the initial input stress model.

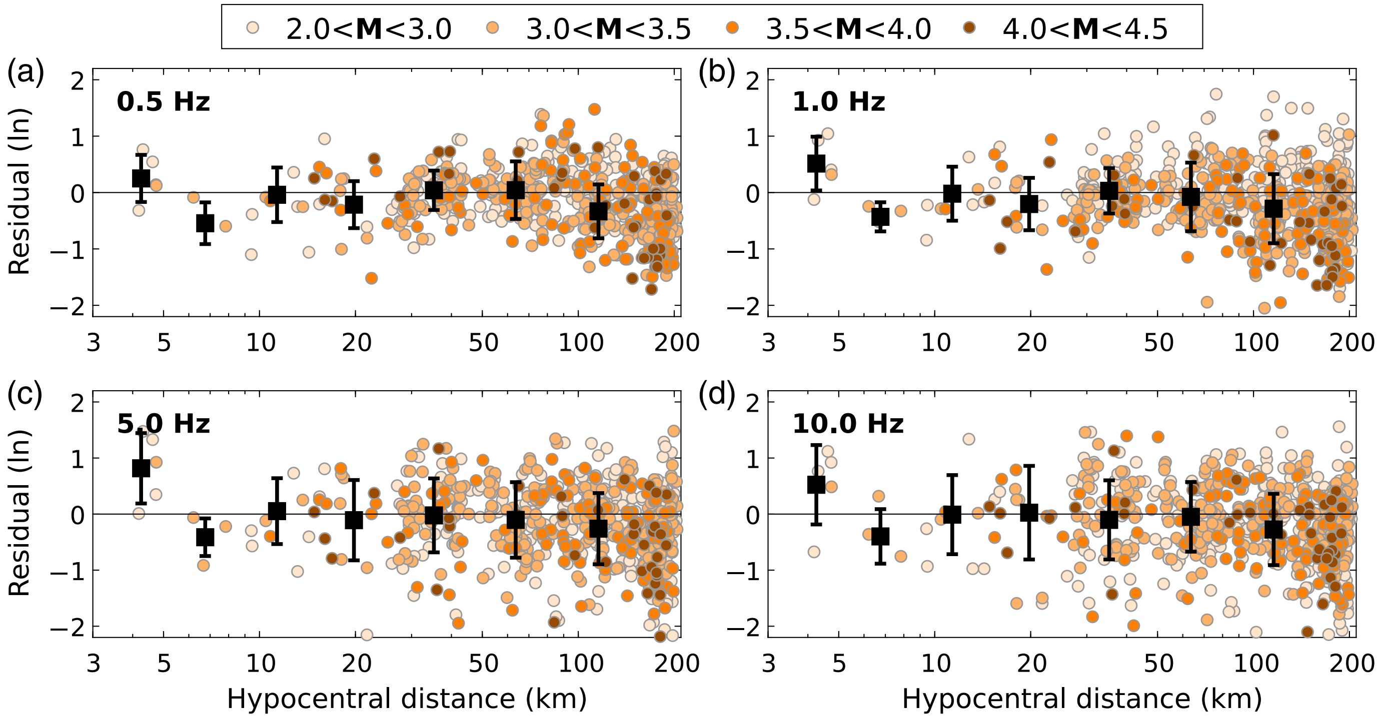

Figure 7. Final residuals for the WCSB GMPE for four oscillator frequencies: (a) 0.5, (b) 1.0, (c) 5.0, and (d) 10.0 Hz. The residuals are shaded based on magnitude, where darker circles are higher magnitude events. Squares show mean residuals and their standard deviation in log-spaced distance bins. The color version of this figure is available only in the electronic edition.

RESULTS

GMPE residuals and directivity effects

The final residuals for the modified WCSB GMPE are shown in Figure 7. No dependence on magnitude or distance is observed, with the possible exception of a sparsely defined positive trend at high frequencies at very close distances. Holmgren *et al.* (2019) found that f_c varied significantly with station azimuth for about half of the earthquakes in the WCSB, despite their relatively small magnitude. To investigate the effect of directivity on response spectral amplitudes, we partition the residuals from Figure 7 into their corresponding between-event and within-event terms. The between-event term represents the average difference between an event's source term and the median prediction of the GMPE, whereas the within-event term is each record's offset relative to the GMPE after correcting for the between-event term (Al Atik *et al.*, 2010). To study azimuthal effects, we are interested in the within-event component. As shown in Figure 8, we find that directivity effects are observable in response spectra residuals for these events for the higher oscillator frequencies. We note that no residual trends in azimuth were observed for frequencies <1.0 Hz (Fig. 8 shows an example for 1.0 Hz; plots for lower frequencies look similar). For frequencies >5 Hz, stations located in the forward rupture direction (azimuth relative to rupture direction of <90°) tend to have larger PSA values than predicted by the GMPE, whereas the opposite is true for stations in the backward rupture direction (azimuth >90°). This effect is on average 0.38 ln units (i.e., a factor of 1.5) in the forward direction and −0.34 ln units in the backward direction. There is also a slight dependence on distance; for example, records at ≤50 km had a larger forward directivity effect (factor of 1.8), in comparison to records at >150 km (factor of 1.2). This may partially explain the slight positive trend in high-frequency residuals at close distances—they may be more influenced by directivity effects. Overall, we conclude that the residuals are higher in the forward rupture direction and lower in the opposite direction.

Stress parameter versus stress-drop values

Figure 9 displays the stress parameters for all events, as obtained from the region-specific GMPE. On average, the stress parameters and corresponding stress-drop values from the Holmgren *et al.* (2019) spectral ratio study follow a 1:1 trend (Fig. 9b), albeit with significant event-to-event scatter. This correspondence is consistent with our defined input stress model to the GMPE development; recall that we defined the input stress model from the EGF stress-drop values, scaled slightly so as to obtain a 1:1 trend on average (input model of Fig. 2). Figure 9 also shows the recovered values of $\Delta\sigma_{par}$ in comparison with those of our input model ($\Delta\sigma_{model}$).

Figure 10 shows the Brune f_c values from the GMPE inversion compared to the EGF f_c results, plotted against magnitude. It can be seen that the EGF f_c values from Holmgren *et al.* (2019) tend to be broadly scattered over all corner frequencies, whereas the GMPE f_c values are scattered

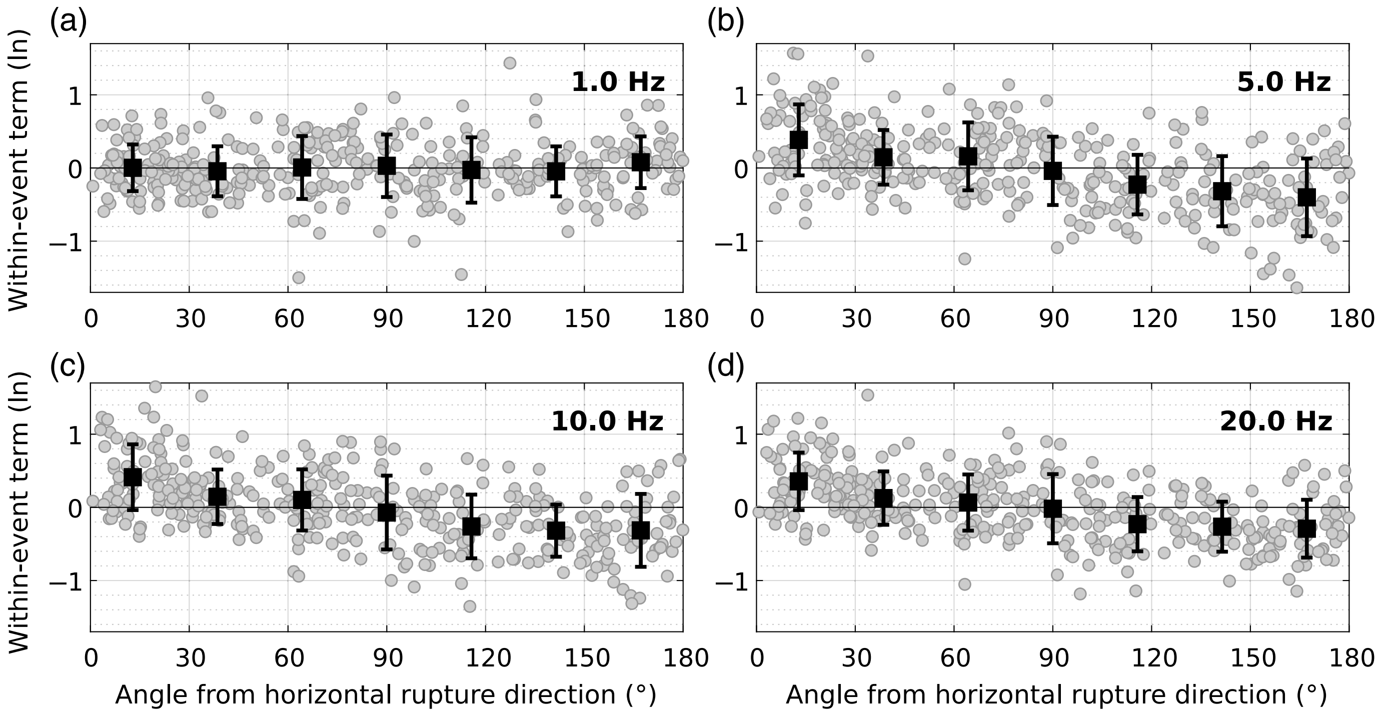

Figure 8. Within-event residuals (circles) for the 39 earthquakes with resolvable directivity effects. The residuals are sorted and plotted versus the relative angle with respect to the rupture direction, where 0° records are from stations in the forward rupture direction and 180° records are from stations in the backward direction. Four oscillator frequencies are plotted: (a) 1.0, (b) 5.0, (c) 10.0, and (d) 20.0 Hz. The mean and standard deviations in azimuth bins are plotted as black squares and vertical horizontal bars.

primarily below 3.0 Hz. We believe that this reflects the lack of ability of the GMPE approach to adequately recover high-frequency source attributes; the strong site-effect issues noted at higher frequencies often obscure the corner frequency. Table S1 contains the final earthquakes' EGF and GMPE f_c values.

DISCUSSION

We developed a region-specific GMPE for the WCSB calibrated to response spectra data, assuming a Brune source model with attributes taken from an EGF study for the same region. Event-specific estimates of $\Delta\sigma_{par}$ obtained by fitting amplitudes to the GMPE are consistent with the corresponding values of $\Delta\sigma_{drop}$ from the EGF study, but there is significant scatter between estimates. This may partly reflect that $\Delta\sigma_{par}$ is dependent to some extent on both the low- and high-frequency portions of the Fourier spectra (Bora *et al.*, 2016; Bindi *et al.*, 2017), and thus the stress parameter does not have the same physical meaning as the stress drop. Another major difference between the two methods is that the EGF method accounts for the path and site effects through spectral division, whereas the GMPE method is based on empirically determined average path and site effects in the region. Ide *et al.* (2003) compared stress-drop estimates obtained from the EGF method to those obtained from single-event Fourier spectral fitting and found that the EGF method tends to produce higher values of stress drop. They linked the mismatch between the two methods to the trade-off between source and attenuation models when fitting the Fourier spectra of individual events. Boore *et al.* (2010) also noted the dependence of the stress parameter values on attenuation models in their stochastic-modeling study. In the development of the WCSB GMPE in this study, we used the regional geometric spreading F_Z and anelastic attenuation F_γ models from Novakovic *et al.* (2019). These were derived through empirical analysis of WCSB earthquakes. Similarly, the final calibration factor C and station terms F_S were also derived empirically based on the residuals (equation 5). The simultaneous solution for parameter coefficients is nonunique and represents only the gross average characteristics of the underlying processes. By contrast, the EGF method is more effective in isolating the source effects, although it does require a good selection of EGF events of appropriate mechanism, location, and size. A lack of suitable EGF earthquakes can lead to biased estimates of f_c (e.g., Abercrombie, 2015; Wu and Chapman, 2017). For example, because EGF earthquakes are small, they have low SNR and may have significant bandwidth limitations. This limits the number of useable stations and may lead to large gaps in azimuthal coverage (Holmgren *et al.*, 2019; Shearer *et al.*, 2019). The GMPE method avoids this limitation because it does not require the availability of smaller EGF events; for the GMPE method, we require sufficient SNR only for the target earthquakes.

To further investigate how EGF $\Delta\sigma_{drop}$ and GMPE $\Delta\sigma_{par}$ differ, we compare the ratios between individual record

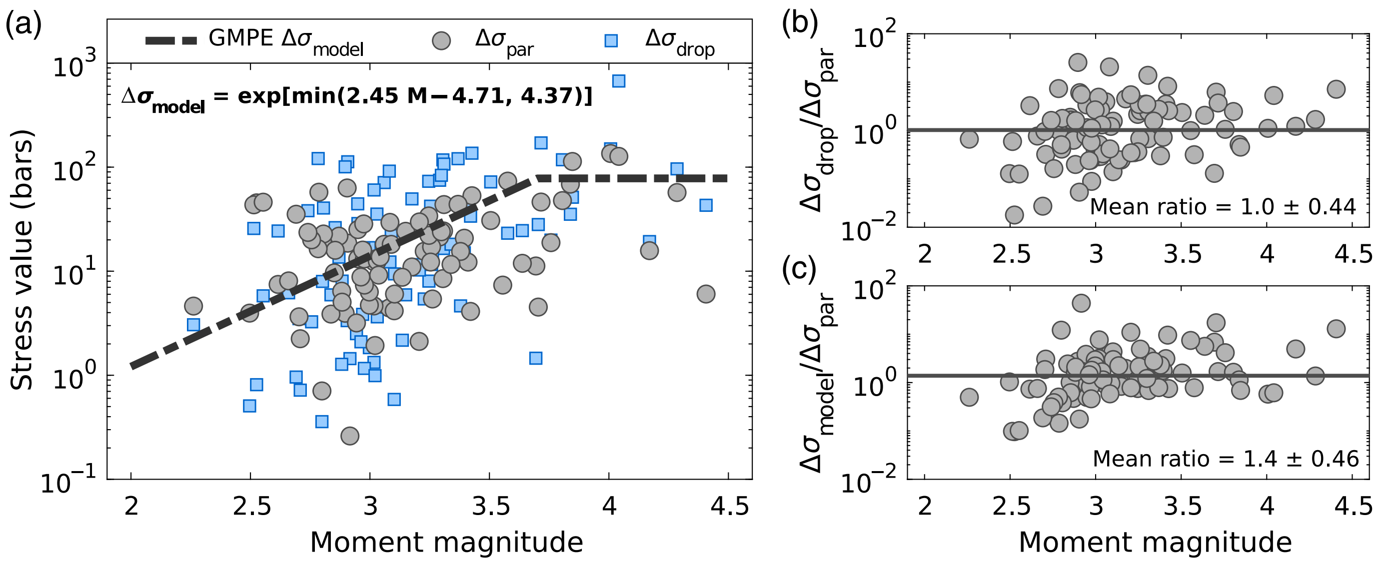

Figure 9. (a) Earthquake stress parameters plotted against moment magnitude (circles). The EGF stress drops from Holmgren *et al.* (2019) are also shown (squares), along with the stress model for WCSB GMPE ($\Delta\sigma_{model}$). (b) Ratios between EGF stress drops and GMPE stress parameters plotted against moment magnitude. (c) Ratios between $\Delta\sigma_{model}$ and the event-specific GMPE stress parameters plotted against moment magnitude. The color version of this figure is available only in the electronic edition.

EGF f_c and GMPE f_c. The ratios were divided into bins to examine different source parameters. Using the Student's t-test (Student, 1908), no statistical significance was found when comparing mean ratios for different magnitude bins or different hypocentral distance bins. However, we observe differences in results related to the rupture direction when comparing EGF and GMPE f_c values. Figure 11 shows the ratio of EGF record f_c to GMPE f_c as a function of angle from rupture direction for the 39 earthquakes with resolvable directivity, color coded based on the relative station azimuth to the horizontal rupture direction (in which 0° is the rupture direction). For stations located in the forward rupture direction (0° ± 45°), the EGF method tends to produce higher f_c measurements, with a geomean and standard error of 1.6 ± 0.2. On the other hand, for stations located in the backward rupture direction (180° ± 45°), the two methods produced similar f_c values with a geomean and standard error of 0.9 ± 0.2. This suggests that the GMPE method may underestimate corner frequency for records with enhanced high-frequency content due to forward directivity. The rich high-frequency content in the forward directivity azimuths is filtered by path and site effects in the GMPE method, making it difficult to obtain the true corner. The GMPE method does recover some indication of directivity (as seen by the within-event residuals in Fig. 8), but it is smeared out relative to that seen by the EGF method. We also investigated whether using only posthole or surface stations impacted the EGF–GMPE f_c ratios. No significant difference was found in the recovered values of corner frequency when subdivided based on station type, indicating that these effects were successfully removed through the station terms F_S.

Baltay *et al.* (2013) used natural earthquakes to compare stress drops obtained using the EGF method to a_{rms} stress parameters obtained from the acceleration Fourier spectrum.

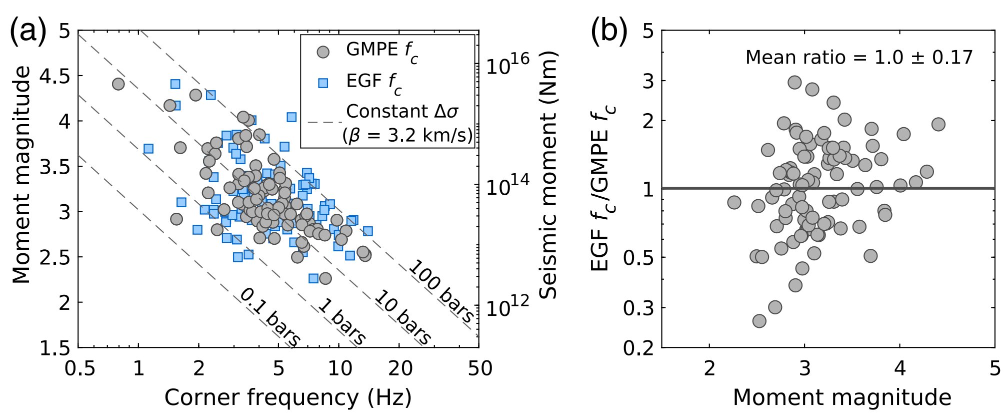

Figure 10. (a) Corner frequencies obtained through GMPE inversion (circles) and through the EGF method (squares), plotted against magnitude. Constant stress value lines using equation (6) are shown. Note that the values of the stress-drop lines depend heavily on the convention used to link corner frequency to stress drop, as described in the Stress Parameter $\Delta\sigma_{par}$ section. (b) Ratios between the EGF and GMPE corner frequencies. The color version of this figure is available only in the electronic edition.

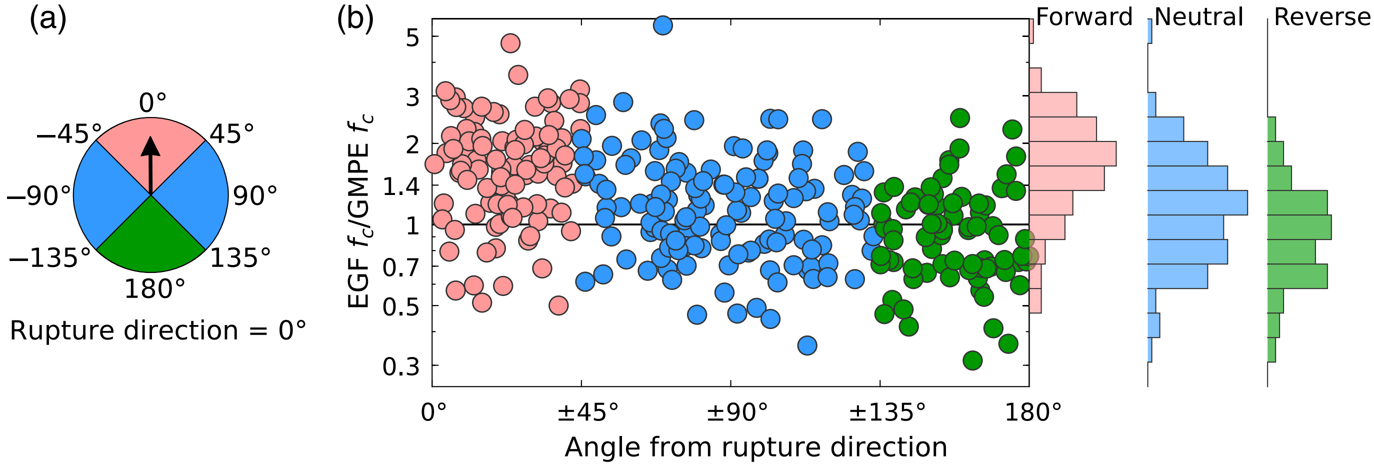

Figure 11. Comparison of f_c by record between the EGF and the GMPE methods. (a) Schematic view of the three azimuth quadrants with respect to horizontal rupture direction: records within 0° ± 45° are in the forward direction; records within 180° ± 45° are in the backward direction; and remaining records are in the neutral direction. (b) Ratios of EGF f_c to GMPE f_c (circles) plotted as a function of horizontal angle away from rupture direction, shaded based on quadrant from (a). Histograms showing the ratio distributions can be seen on the right. The color version of this figure is available only in the electronic edition.

They found that the two methods produced comparable estimates of stress for earthquakes with $\mathbf{M} \geq 3.0$ at close distances ($R \leq 20$ km). The a_{rms} method requires that the cutoff frequency $f_{\max}$ (Hanks, 1982) be sufficiently larger than f_c, which only occurs for relatively large earthquakes at close distances. Considering the sparse regional station coverage and lack of data within 20 km (30 records out of 643 in total), the a_{rms} method is not applicable for this region.

The variability in the values of $\Delta\sigma_{\mathrm{par}}$ is slightly less than that for $\Delta\sigma_{\mathrm{drop}}$, as seen in Figure 9. The $\Delta\sigma_{\mathrm{par}}$ distribution has a standard deviation of 1.1 natural-log units, whereas the $\Delta\sigma_{\mathrm{drop}}$ variability is 1.6 natural-log units. Cotton *et al.* (2013) compared $\Delta\sigma_{\mathrm{par}}$ distributions from the between-event terms of GMPE studies to $\Delta\sigma_{\mathrm{drop}}$ values from source studies that determined corner frequency, and found that the GMPE $\Delta\sigma_{\mathrm{par}}$ variabilities were much lower than those for $\Delta\sigma_{\mathrm{drop}}$ (0.3–0.6 ln units for $\Delta\sigma_{\mathrm{par}}$ vs. 0.6–1.8 for $\Delta\sigma_{\mathrm{drop}}$). The larger variability for $\Delta\sigma_{\mathrm{drop}}$ is partly due to its dependence on f_c^3 (equation 6); a small error in f_c will lead to a large error in $\Delta\sigma_{\mathrm{drop}}$. Our results are consistent with this finding. Our $\Delta\sigma_{\mathrm{par}}$ variability is larger than that obtained by Cotton *et al.* (2013), perhaps because we compute stress parameter by fitting the GMPE to the entire response spectrum, whereas Cotton *et al.* (2013) used a single ground-motion measure (i.e., PGA). Overall, we note that both our $\Delta\sigma_{\mathrm{drop}}$ and $\Delta\sigma_{\mathrm{par}}$ variabilities are large relative to those observed in other studies (e.g., Oth *et al.*, 2017). This may reflect a combination of effects, including higher source variability in the attributes of events induced by hydraulic fracturing, and complex path and site effects, including directivity, that interact with a sparse station distribution. Holmgren *et al.* (2019) noted that 21 out of 92 earthquakes displayed source complexity in the form of deviations from a typical Brune model, likely due to rupture of multiple faults (Wang *et al.*, 2018; Eyre *et al.*, 2019). Resolvable directivity was observed for 39 out of the 92 earthquakes, which led to an average f_c difference of a factor of 4 depending on azimuth (Holmgren *et al.*, 2019). Forty of the 92 earthquakes did not have sufficient station coverage to determine directivity. Therefore, there could be a significant bias in the f_c estimates due to directivity effects, leading to large $\Delta\sigma_{\mathrm{drop}}$ and $\Delta\sigma_{\mathrm{par}}$ variability.

In this study, we developed our GMPE using a stress model that explicitly assumed a relationship between the values of the stress parameter and the EGF stress drop (Fig. 2); the input stress model to the GMPE was a slightly scaled (factor of 1.3) version of a line fit to the EGF stress-drop values. We examined the sensitivity of results to this assumption. Interestingly, changing the initial stress model affects the final calibration factor C, but not the site terms F_S or the overall residuals between the GMPE and observed data. Any mismatch between the ideal form of the stress model and that assumed in the GMPE development is mapped entirely into C. This means that the stress model does not need to be known in advance of developing a regional-specific GMPE, but can either be obtained through fitting a model to stress drops from an existing source study in the region, or by simply assuming a constant 100 bars from the default source model (Yenier and Atkinson, 2015a). Specifically, we repeated the GMPE development assuming an input stress model of 100 bars for all events; the inversion returned the same site terms and residuals as reported here; only the calibration function and stress parameter values changed. If a stress model producing $\Delta\sigma_{\mathrm{par}}$ similar to published $\Delta\sigma_{\mathrm{drop}}$ is preferred, the stress model (starting initially with 100 bars, or with a $\Delta\sigma_{\mathrm{drop}}$ model from EGF studies as was done here) can be iterated until $\Delta\sigma_{\mathrm{par}}$ and $\Delta\sigma_{\mathrm{drop}}$ are consistent.

CONCLUSIONS

We develop a region-specific GMPE for induced earthquakes in WCSB of **M** 2.3–4.4 to distances of 200 km using published EGF stress-drop estimates ($\Delta\sigma_{\text{drop}}$) as a proxy for an input stress parameter ($\Delta\sigma_{\text{par}}$) model. The use of the generic GMPE model ensures reasonable scaling of motions to larger magnitudes (Yenier and Atkinson, 2015a). By constraining the input stress model to approximately follow the results from EGF source studies, we ensured agreement on average between the GMPE- and EGF-based values of stress. Moreover, our approach recognizes that EGF-based source parameters are inherently more robust (when available). We compared individual earthquake $\Delta\sigma_{\text{par}}$ estimates obtained by fitting response spectra to the GMPE to $\Delta\sigma_{\text{drop}}$ values to investigate differences between the parameters. Significant event-to-event variability is found, which we attribute to: (1) response spectra and Fourier spectra are not linearly related, and thus $\Delta\sigma_{\text{drop}}$ and $\Delta\sigma_{\text{par}}$ values are not directly equivalent (Bora *et al.*, 2016); (2) GMPEs are nonunique due to trade-offs between parameters, which represent only average regional effects, and are thus inherently limited in their ability to resolve source parameters. In particular, we noted that the GMPE method returned lower f_c estimates than the EGF method in the forward rupture direction, while returning similar values in the backward direction.

When using estimates of stress drop to infer high-frequency amplitudes of ground motion, the conventions linking stress drop to corner frequency are critical. It is best to consider corner frequency as the fundamental ground-motion parameter controlling high-frequency content. Moreover, it should be noted that directivity effects can exert a profound effect on corner frequency, in both the EGF and GMPE approaches, and thus source parameters estimated from a sparse station distribution may be highly uncertain. Nonetheless, we have shown that $\Delta\sigma_{\text{drop}}$ from EGF studies can be used as an input $\Delta\sigma_{\text{par}}$ model in GMPE development. This also allows the possibility of using a distribution of $\Delta\sigma_{\text{drop}}$ values from published studies available in the literature when developing region-specific GMPEs.

DATA AND RESOURCES

We use the database from Holmgren *et al.* (2019), which is based on three different earthquake catalogs: the Composite Alberta Seismicity Catalogue (https://www.inducedseismicity.ca/catalogues, last accessed July 2019), the Geological Survey of Canada catalog (Visser *et al.*, 2017), and the Alberta Geological Survey catalog (Stern *et al.*, 2018). Incorporated Research Institutions for Seismology (IRIS) was used to download time series from the following networks: Canadian National Seismograph Network (CN, Geological Survey of Canada, 1989), Regional Alberta Observatory for Earthquake Studies Network (RV, Alberta Geological Survey/Alberta Energy Regulator, 2013), TransAlta Monitoring Network (TD), and Canadian Rockies and Alberta Network (Y5). Signal processing was done using MATLAB (www.mathworks.com/products/matlab, last accessed January 2018). The supplemental material of this article contains four tables. Table S1 contains parameters of the earthquakes studies; Table S2 contains the 5% damped pseudospectral acceleration (PSA) of the records used in the study; Table S3 lists the coefficients to the western Canada sedimentary basin (WCSB) ground-motion prediction equation (GMPE); and Table S4 contains the individual station terms used in the WCSB GMPE.

ACKNOWLEDGMENTS

The authors thank Associate Editor Delphine Fitzenz and two anonymous reviewers for their helpful comments. The Natural Sciences and Engineering Research Council of Canada, TransAlta, and Nanometrics funded this work.

REFERENCES

Abercrombie, R. E. (2015). Investigating uncertainties in empirical Green's function analysis of earthquake source parameters, *J. Geophys. Res.* **120,** no. 6, 4263–4277.

Abercrombie, R. E., S. Bannister, J. Ristau, and D. I. Doser (2017). Variability of earthquake stress drop in a subduction setting, the Hikurangi Margin, New Zealand, *Geophys. J. Int.* **208,** no. 1, 306–320.

Al Atik, L., N. A. Abrahamson, J. J. Bommer, F. Scherbaum, F. Cotton, and N. M. Kuehn (2010). The variability of ground-motion prediction models and its components, *Seismol. Res. Lett.* **81,** no. 5, 794–801.

Allmann, B. P., and P. M. Shearer (2009). Global variations of stress drop for moderate to large earthquakes, *J. Geophys. Res.* **114,** no. 1, 1–22.

Anderson, J. G., and S. E. Hough (1984). A model for the shape of the Fourier amplitude spectrum of acceleration at high frequencies, *Bull. Seismol. Soc. Am.* **74,** no. 5, 1969–1993.

Atkinson, G. M. (2004). Empirical attenuation of ground-motion spectral amplitudes in southeastern Canada and the northeastern United States, *Bull. Seismol. Soc. Am.* **94,** no. 3, 1079–1095.

Atkinson, G. M., and I. A. Beresnev (1997). Don't call it stress drop, *Seismol. Res. Lett.* **68,** no. 1, 3–4.

Atkinson, G. M., and D. M. Boore (1997). Stochastic point-source modeling of ground motions in the Cascadia region, *Seismol. Res. Lett.* **68,** no. 1, 74–85.

Atkinson, G. M., and D. M. Boore (2006). Earthquake ground-motion prediction equations for eastern North America, *Bull. Seismol. Soc. Am.* **96,** no. 6, 2181–2205.

Atkinson, G. M., and R. F. Mereu (1992). The shape of ground motion attenuation curves in southeastern Canada, *Bull. Seismol. Soc. Am.* **82,** no. 5, 2014–2031.

Atkinson, G. M., D. W. Eaton, H. Ghofrani, D. Walker, B. Cheadle, R. Schultz, R. Shcherbakov, K. Tiampo, Y. J. Gu, R. M. Harrington, *et al.* (2016). Hydraulic fracturing and seismicity in the western Canada sedimentary basin, *Seismol. Res. Lett.* **87,** no. 3, 631–647.

Atkinson, G. M., B. Hassani, A. Singh, E. Yenier, and K. Assatourians (2015). Estimation of moment magnitude and stress parameter from ShakeMap ground-motion parameters, *Bull. Seismol. Soc. Am.* **105,** no. 5, 2572–2588.

Baltay, A. S., T. C. Hanks, and G. C. Beroza (2013). Stable stress-drop measurements and their variability: Implications for ground-motion prediction, *Bull. Seismol. Soc. Am.* **103,** no. 1, 211–222.

Baltay, A. S., G. A. Prieto, and G. C. Beroza (2010). Radiated seismic energy from coda measurements and no scaling in apparent stress with seismic moment, *J. Geophys. Res.* **115,** no. 8, 1–12.

Bindi, D., D. Spallarossa, and F. Pacor (2017). Between-event and between-station variability observed in the Fourier and response spectra domains: Comparison with seismological models, *Geophys. J. Int.* **210,** no. 2, 1092–1104.

Boatwright, J., and L. Seekins (2011). Regional spectral analysis of three moderate earthquakes in northeastern North America, *Bull. Seismol. Soc. Am.* **101,** no. 4, 1769–1782.

Boore, D. M. (1983). Stochastic simulation of high-frequency ground motions based on seismological models of the radiated spectra, *Bull. Seismol. Soc. Am.* **73,** no. 6, 1865–1894.

Boore, D. M. (2003). Simulation of ground motion using the stochastic method, *Pure Appl. Geophys.* **160,** nos. 3/4, 635–676.

Boore, D. M., K. W. Campbell, and G. M. Atkinson (2010). Determination of stress parameters for eight well-recorded earthquakes in eastern North America, *Bull. Seismol. Soc. Am.* **100,** no. 4, 1632–1645.

Bora, S. S., F. Scherbaum, N. M. Kuehn, and P. J. Stafford (2016). On the relationship between Fourier and response spectra: Implications for the adjustment of empirical ground-motion prediction equations (GMPEs), *Bull. Seismol. Soc. Am.* **106,** no. 3, 1235–1253.

Brune, J. N. (1970). Tectonic stress and the spectra of seismic shear waves from earthquakes, *J. Geophys. Res.* **75,** no. 26, 4997–5009.

Campbell, K. W. (2003). Prediction of strong ground motion using the hybrid empirical method and its use in the development of ground-motion (attenuation) relations in eastern North America, *Bull. Seismol. Soc. Am.* **93,** no. 3, 1012–1033.

Chávez, D. E., and K. F. Priestley (1986). Measurement of frequency dependent *Lg* attenuation in the Great Basin, *Geophys. Res. Lett.* **13,** no. 6, 551–554.

Chen, Y., Y. J. Gu, R. M. H. Dokht, and M. D. Sacchi (2015). Crustal imprints of Precambrian orogenesis in western Laurentia, *J. Geophys. Res.* **120,** 6993–7012.

Cotton, F., R. J. Archuleta, and M. Causse (2013). What is sigma of the stress drop? *Seismol. Res. Lett.* **84,** no. 1, 42–48.

Eaton, D. W., N. Igonin, A. Poulin, R. Weir, H. Zhang, S. Pellegrino, and G. Rodriguez (2018). Induced seismicity characterization during hydraulic-fracture monitoring with a shallow-wellbore geophone array and broadband sensors, *Seismol. Res. Lett.* **89,** no. 5, 1641–1651.

Eshelby, J. D. (1957). The determination of the elastic field of an ellipsoidal inclusion, and related problems, *Proc. Math. Phys. Sci.* **241,** no. 1226, 376–396.

Eyre, T. S., D. W. Eaton, M. Zecevic, D. D'Amico, and D. Kolos (2019). Microseismicity reveals fault activation before M_w 4.1 hydraulic-fracturing induced earthquake, *Geophys. J. Int.* **218,** no. 1, 534–546, doi: 10.1093/gji/ggz168.

Farrugia, J. J., S. Molnar, and G. M. Atkinson (2017). Noninvasive techniques for site characterization of Alberta seismic stations based on shear-wave velocity, *Bull. Seismol. Soc. Am.* **107,** no. 6, 2885–2902.

Gupta, I. N., and K. L. McLaughlin (1987). Attenuation of ground motion in the eastern United States, *Bull. Seismol. Soc. Am.* **77,** no. 2, 366–383.

Hanks, T. C. (1979). b values and $\omega^{-\gamma}$ seismic source models: Implications for tectonic stress variations along active crustal fault zones and the estimation of high-frequency strong ground motion, *J. Geophys. Res.* **84,** no. B5, 2235–2242, doi: 10.1029/JB084iB05p02235.

Hanks, T. C. (1982). $f_{\max}$, *Bull. Seismol. Soc. Am.* **72,** no. 6, 1867–1879.

Hanks, T. C., and R. K. McGuire (1981). The character of high-frequency strong ground motion, *Bull. Seismol. Soc. Am.* **71,** no. 6, 2071–2095.

Haskell, N. A. (1964). Total energy and energy spectral density of elastic wave radiation from propagating faults, *Bull. Seismol. Soc. Am.* **54,** no. 6, 1811–1841.

Héloïse, C., P.-Y. Bard, and A. Rodriguez-Marek (2012). Site effect assessment using KiK-net data: Part 1. A simple correction procedure for surface/downhole spectral ratios, *Bull. Earthq. Eng.* **10,** no. 2, 421–448.

Hollender, F. (2019). *Improvement of Practices for a More Robust Site-Specific Seismic Hazard Assessment*, Université Grenoble Alpes, Grenoble, France.

Holmgren, J. M., G. M. Atkinson, and H. Ghofrani (2019). Stress drops and directivity of induced earthquakes in the western Canada sedimentary basin, *Bull. Seismol. Soc. Am.* **109,** no. 5, 1635–1652.

Huang, Y., G. C. Beroza, and W. L. Ellsworth (2016). Stress drop estimates of potentially induced earthquakes in the Guy–Greenbrier sequence, *J. Geophys. Res.* **121,** 1–11.

Ide, S., G. C. Beroza, S. G. Prejean, and W. L. Ellsworth (2003). Apparent break in earthquake scaling due to path and site effects on deep borehole recordings, *J. Geophys. Res.* **108,** no. B5, ESE 16-1–ESE 16-13.

Nigam, N. C., and P. C. Jennings (1969). Calculation of response spectra from strong-motion earthquake records, *Bull. Seismol. Soc. Am.* **59,** no. 2, 909–922.

Novakovic, M., G. M. Atkinson, and K. Assatourians (2018). Empirically calibrated ground-motion prediction equation for Oklahoma, *Bull. Seismol. Soc. Am.* **108,** no. 5, 2444–2461.

Novakovic, M., G. M. Atkinson, K. Assatourians, and Y. J. Gu (2019). Empirical characterization of ground motions for induced seismicity in Alberta, *12th Canadian Conf. on Earthquake Engineering*, Quebec City, Canada, 17–20 June 2019.

Onwuemeka, J., Y. Liu, and R. M. Harrington (2018). Earthquake stress drop in the Charlevoix Seismic Zone, eastern Canada, *Geophys. Res. Lett.* **45,** no. 22, 12,226–12,235.

Oth, A. P. H., H. Miyake, and D. Bindi (2017). On the relation of earthquake stress drop and ground motion variability, *J. Geophys. Res.* **122,** no. 7, 5474–5492.

Pezeshk, S., A. Zandieh, K. W. Campbell, and B. Tavakoli (2018). Ground-motion prediction equations for central and eastern North America using the hybrid empirical method and NGA-West2 empirical ground-motion models, *Bull. Seismol. Soc. Am.* **108,** no. 4, 2278–2304.

Schultz, R., R. Wang, Y. J. Gu, K. Haug, and G. M. Atkinson (2017). A seismological overview of the induced earthquakes in the Duvernay play near Fox Creek, Alberta, *J. Geophys. Res.* **122,** no. 1, 492–505.

Shearer, P. M., R. E. Abercrombie, D. T. Trugman, and W. Wang (2019). Comparing EGF methods for estimating corner frequency and stress drop from P wave spectra, *J. Geophys. Res.* **124,** no. 4, 3966–3986, doi: 10.1029/2018JB016957.

Stern, V., R. Schultz, L. Shen, Y. J. Gu, and D. W. Eaton (2018). Alberta earthquake catalogue, version 6.0 (GIS data, point features), *Alberta Energy Regulator, AER/AGS Digital Dataset 2013-0017*, https://ags.aer.ca/publications/DIG_2013_0017.html (last accessed April 2019).

Student (1908). The probable error of a mean, *Biometrika* 1–25.

Sumy, D. F., C. J. Neighbors, E. S. Cochran, and K. M. Keranen (2017). Low stress drops observed for aftershocks of the 2011 M_w 5.7 Prague, Oklahoma, earthquake, *J. Geophys. Res.* **122,** no. 5, 3813–3834.

Toro, G. R., and R. K. McGuire (1987). An investigation into earthquake ground motion characteristics in eastern North America, *Bull. Seismol. Soc. Am.* **77,** no. 2, 468–489.

Visser, R., B. Smith, H. Kao, A. B. Mahani, J. Hutchinson, and J. E. McKay (2017). A comprehensive earthquake catalogue for northeastern British Columbia and western Alberta, 2014–2016, *Geol. Surv. of Canada, Open File 8335*, 1.zip File, doi: 10.4095/306292.

Wang, R., Y. J. Gu, R. Schultz, and Y. Chen (2018). Faults and non-double-couple components for induced earthquakes, *Geophys. Res. Lett.* **45,** no. 17, 8966–8975.

Wu, Q., and M. Chapman (2017). Stress-drop estimates and source scaling of the 2011 mineral, Virginia, mainshock and aftershocks, *Bull. Seismol. Soc. Am.* **107,** no. 6, 2703–2720, doi: 10.1785/0120170098.

Yenier, E., and G. M. Atkinson (2015a). An equivalent point-source model for stochastic simulation of earthquake ground motions in California, *Bull. Seismol. Soc. Am.* **105,** no. 3, 1435–1455.

Yenier, E., and G. M. Atkinson (2015b). Regionally adjustable generic ground-motion prediction equation based on equivalent point-source simulations: Application to central and eastern North America, *Bull. Seismol. Soc. Am.* **105,** no. 4, 1989–2009.

Yoshimitsu, N., W. L. Ellsworth, and G. C. Beroza (2019). Robust stress drop estimates of potentially induced earthquakes in Oklahoma: Evaluation of empirical Green's function, *J. Geophys. Res.* **124,** 1–13.

Manuscript received 3 December 2019
Published online 31 March 2020